Tunneling spectroscopy of mixed stable-chaotic electron dynamics in a quantum well

T. M. Fromhold,[1] P. B. Wilkinson,[1] R. K. Hayden,[1,2] L. Eaves,[1] F. W. Sheard,[1] N. Miura,[2] and M. Henini[1]
[1]*School of Physics and Astronomy, University of Nottingham NG7 2RD, United Kingdom*
[2]*Institute for Solid State Physics, University of Tokyo, 5-1-5 Kashiwanoha, Kashiwa, Chiba 277-8581, Japan*
(Received 7 September 2001; revised manuscript received 28 November 2001; published 28 March 2002)

Experimental and theoretical studies of mixed stable-chaotic electron dynamics in the quantum well of a resonant tunneling diode are reported. The classical orbits of electrons injected into the well from an emitter accumulation layer change from regular to chaotic when an applied magnetic field is tilted away from the normal to the well walls. In the regime of mixed stable-chaotic electron dynamics, we identify a period-tripling bifurcation, which, in contrast to previous experiments, is directly accessible to the tunneling electrons. Stable classical orbits associated with this bifurcation are related directly to the wave functions of the quantum well using a Wigner function analysis. There is a striking similarity between the form of the electron Wigner functions and the corresponding classical Poincaré sections. This allows us to identify subsets of quantum well states associated with stable orbits around the period-tripling bifurcation. These states control the flow of electrons through the device and produce a series of strong resonant peaks in the measured current-voltage characteristics. We also identify resonant features associated with ''scarred'' quantum well states in which the probability density is concentrated along an unstable but periodic classical path.

DOI: 10.1103/PhysRevB.65.155312 PACS number(s): 73.21.−b, 05.45.Mt, 73.40.Gk, 73.40.Kp

I. INTRODUCTION

Understanding the behavior of quantum systems with chaotic classical dynamics continues to stimulate a great deal of research activity in diverse areas of physical science and mathematics.[1] The first experimental studies of such systems were performed on highly excited hydrogenic atoms.[2–9] Over the past 10 years, advances in the laser cooling of atoms[10–20] and in the fabrication of high-quality semiconductor nanostructures[21–50] have provided new directions for experimental quantum chaology. Analogous electromagnetic wave phenomena have been investigated in microwave billiards[51–53] and optical cavities with chaotic ray dynamics.[54–56] In semiconductor physics, chaotic electron transport has been studied in two-dimensional billiard structures,[21–26] antidot arrays,[27] superlattices,[28–31] and in resonant tunneling diodes (RTDs) containing a wide quantum well (QW),[32–50] which are the subject of this paper.

An electron moving in a QW follows regular classical paths when a magnetic field B is applied perpendicular to the well walls.[32–50] These stable orbits are characterized by two frequencies: $\omega_T = 2\pi/T$, where T is the period for a one-dimensional return trip across the well, and the angular frequency ω_c for cyclotron motion about the magnetic-field axis. Tilting the magnetic field at an angle θ to the normal to the well walls has a pronounced effect on the classical orbits and corresponding quantized states.[32–50] In particular, increasing θ from zero induces a changeover from stable regular motion to strong classical chaos. This transition proceeds via a complex series of orbital bifurcations that occur whenever $n\omega_T = p\omega_c \cos\theta$, where n, and p are integers.[34–36,41,43,44,46–48]

When the QW is incorporated in a double-barrier RTD, the effect of chaotic electron dynamics on the corresponding quantized states of the QW can be investigated using tunneling spectroscopy experiments.[32–34,36,37] In these experiments, the current I due to tunneling transitions from a two-dimensional electron gas (2DEG) in the emitter accumulation layer (see Fig. 1) is measured as a function of the applied voltage V. When the magnetic field is applied normal to the well walls ($\theta = 0°$), the current-voltage $I(V)$ characteristics of a wide range of RTDs[32,34,36,37] reveal simple series of regularly spaced peaks similar to those observed for $B = 0$, which originate from resonant tunneling into the box-quantized states (two-dimensional subbands[32]) of the well. The physical reason for this simple behavior is that for $\theta = 0°$, the periodic traversing motion across the well is decoupled from the cyclotron motion in the plane of the well. Tilting the magnetic field induces more complex electron dynamics because the magnetic-field component in the plane of the QW couples the traversing and cyclotron motion. For small B and/or a narrow QW, the in-plane magnetic-field component can be treated as a perturbation,[57] and the classical motion remains regular.[32,36] By contrast, for large B and/or a wide QW, the in-plane magnetic field strongly

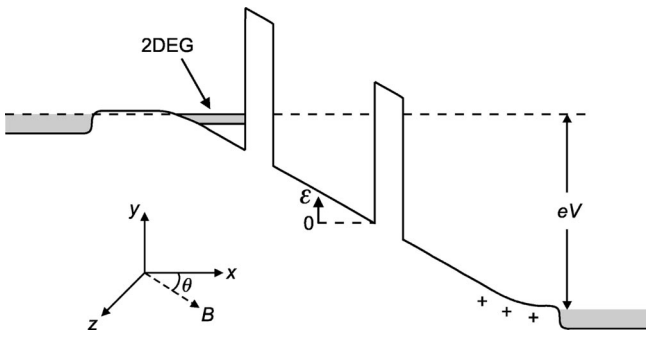

FIG. 1. Schematic conduction-band profile of the RTD under bias V showing emitter 2DEG, electron energy ε measured from conduction-band edge at the right-hand side of QW, and n-doped contacts. Shaded regions show energy ranges of occupied states in 2DEG and heavily doped contact regions when $B = 0$. Crosses represent ionized donors in collector contact. Inset shows orientation of magnetic field relative to the coordinate axes.

couples the traversing and cyclotron motion, thus generating chaotic classical dynamics.[32–50] Despite the onset of chaos, the $I(V)$ characteristics still reveal series of quasiperiodic resonant peaks, though the voltage spacing of these peaks is usually between two and four times smaller than for $\theta=0°$.[32,34,36,37] At first sight, the observation of quasiperiodic current resonances in the regime of strong classical chaos is surprising because the energy-level spectrum is very irregular,[40] and the distribution of nearest-neighbor level spacings follows the Wigner statistics predicted by Random Matrix Theory.[33] However, we have shown[33,37,40] that the $I(V)$ characteristics are controlled by subsets of QW states that are equally spaced in energy and exhibit wave-function ''scarring:'' a concentration of probability density along an unstable but periodic classical path.[58] The current flow is dominated by tunneling into these scarred states, which generate series of quasiperiodic resonant peaks in the $I(V)$ characteristics.[33,37,40] Consequently, the electrical properties of the RTD depend on the particular parameters of the device and applied fields, which shape the periodic orbits and associated scar patterns, rather than the universal energy-level statistics given by Random Matrix Theory.

Experiments performed at very high magnetic fields (i.e., high enough to ensure that $\omega_c \simeq \omega_T$ for a given well width), for which the electrons exhibit strongly chaotic motion, are now well understood.[32,33,37,40,44,45] By contrast, data obtained at lower magnetic-field values, which produce a mixed stable-chaotic classical phase space, are less well understood for two reasons. First, for RTDs there has been no direct comparison between the distribution of stable islands in a mixed stable-chaotic classical phase space and the form of the corresponding quantized states. Second, there is still debate about which parts of the classical phase space are accessible to the tunneling electrons.[39] In our previous work,[32,40] we estimated the momentum spread of electrons entering the QW by considering the initial momentum distribution in the 2DEG, and the momentum transferred by the Lorentz force acting on the tunneling electrons. In the regime of strong classical chaos, this procedure has enabled us to identify correctly those isolated unstable periodic orbits in the QW that generate distinct series of resonant peaks in $I(V)$. But when the electrons are injected into a region of mixed stable-chaotic phase space containing different types of nonisolated stable orbits associated with a bifurcation, and also unstable orbits linked to the hyperbolic points of the bifurcation, it is much more difficult to determine which of these orbits affect the quantized eigenstates and $I(V)$ curves. Existing semiclassical approximations, which relate the tunnel current to particular periodic orbits in the QW,[43,44,48–50] are inapplicable in this regime, because they breakdown at bifurcations.[47–49]

Here, we explore the mixed phase-space case using a RTD containing a narrower QW (of width $w=30$ nm) than in our previous work,[32,33] and higher pulsed magnetic fields up to 42 T. For fixed B and θ, the $I(V)$ characteristics reveal simple series of regularly spaced resonant peaks, which are qualitatively similar to those observed in the regime of strong classical chaos. As B is increased from 0, the voltage spacing of the resonant peaks suddenly falls by a factor ~ 3, at a field value that depends on V. For sufficiently large B, whose magnitude is again determined by V, the voltage spacing increases again to a value similar to that found when $B=0$. The main aim of the paper is to explain these observations. We show that the sudden reduction of the voltage spacings originates from a period-tripling bifurcation in phase space, and relate this bifurcation directly to the quantized states of the well and to the observed tunneling characteristics. This type of bifurcation has been identified previously in the phase space of RTDs containing wider QWs.[35,36,39,40,43,44] But for these earlier structures, the bifurcation was inaccessible to experiment because the Lorentz force associated with the magnetic-field component in the plane of the QW was insufficient to bend the tunneling electron paths into the region of phase space containing the bifurcation. For the narrower QW considered here, ω_T is higher, and so the period-tripling bifurcation corresponding to the resonance condition $\omega_T=3\omega_c \cos\theta$ occurs at higher B values which are sufficient for the electrons to be injected straight into the bifurcation region.[59] We use a Wigner-function analysis to relate the eigenstates of the QW directly to the corresponding classical phase space. This allows us to identify a subset of states, embedded within the full spectrum, which corresponds to two different types of stable orbit associated with the bifurcation. These states produce strong resonant peaks in our calculated $I(V)$ curves, which reproduce all the main features of the experimental data and provide a clear picture of the transition to chaos in the QW.

II. SAMPLE DETAILS AND EXPERIMENTAL ARRANGEMENTS

The RTDs used in our experiments consisted of the following layers, listed in order of growth on a (100) oriented substrate: 2 μm GaAs, heavily n-doped with Si atoms of density $n_D=2\times10^{18}$ cm^{-3}; 50 nm GaAs, $n_D=2\times10^{17}$ cm^{-3}; 50 nm GaAs, $n_D=2\times10^{16}$ cm^{-3}; 10.2 nm GaAs spacer layer, not intentionally doped; 5.7 nm $(Al_{0.4}Ga_{0.6})As$ barrier not intentionally doped; 30 nm GaAs QW, not intentionally doped; 5.7 nm $(Al_{0.4}Ga_{0.6})As$ barrier not intentionally doped; 10.2 nm GaAs spacer layer, not intentionally doped; 50 nm GaAs, $n_D=2\times10^{16}$ cm^{-3}; 50 nm GaAs, $n_D=2\times10^{17}$ cm^{-3}; 500 nm GaAs, $n_D=2\times10^{18}$ cm^{-3}. The material was processed into circular mesas with a diameter of 200 μm and ohmic contacts were made to the top layer and to the substrate. Experiments were performed at a temperature of 4.2 K in a pulsed magnet, which generates fields of up to 42 T. Details of the shape of the magnetic-field pulse have been given previously.[60] Each $I(V)$ characteristic was measured at the peak of the magnetic-field pulse during a time interval less than 0.25 ms, for which the magnetic field is estimated to remain constant within 50 mT. This small variation in the magnetic-field strength has negligible effect on both the measured and calculated $I(V)$ curves.

Figure 1 shows a schematic diagram of the conduction-band profile within the active layers of the device under bias V. A 2DEG accumulates in the undoped spacer layer (emitter contact) adjacent to the left-hand (LH) barrier. The spacer

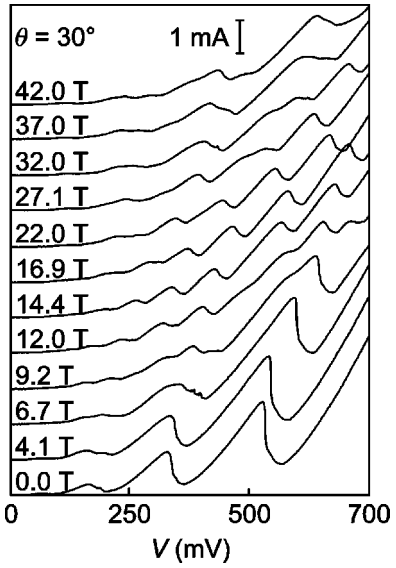

FIG. 2. Experimental $I(V)$ curves (vertically offset for clarity) for $\theta=30°$ and the range of B values indicated. Vertical bar shows current scale.

layer limits the diffusion of dopants into the barrier and QW regions and is four times thicker than in the devices used in some of our previous experiments.[37] This ensures that the QW provides a particularly clean and well-characterized environment for the conduction electrons, relatively free from the effects of ionized donor scattering. Consequently, the resonant peaks observed in $I(V)$ are clearer than in previous samples. Current flows when electrons tunnel from the 2DEG into the quantized states of the QW. Figure 2 shows $I(V)$ curves measured for several magnetic-field values between 0 to 42 T and $\theta=30°$. We focus on this particular parameter range throughout the paper because it is ideal for investigating the effects of orbital bifurcation on experimental tunneling characteristics. When $\theta=0°$ (bottom trace in Fig. 2), the resonant peaks in $I(V)$ originate from Landau-level-index conserving transitions from the single occupied Landau level in the emitter 2DEG into the box-quantized states of the QW. The QW is sufficiently narrow for individual box-quantized states to produce well-resolved resonant peaks in $I(V)$, which we discuss in more detail below. For magnetic fields in the range 12 T $\lesssim B \lesssim$ 22 T, the voltage spacings of the resonant peaks decrease by a factor close to 3. But at higher fields, they increase again to values similar to those observed for $\theta=0°$. To begin our explanation of this behavior, in the following section we consider how the classical phase space of electrons in the QW changes when the applied magnetic field is tilted away from the normal to the well walls.

III. THEORETICAL MODEL AND COMPARISON OF MEASURED AND CALCULATED $I(V)$ CURVES

We have calculated classical orbits for electrons in the QW when there is a uniform electric field $F \propto V$ across the well, and a magnetic field $\mathbf{B}=(B\cos\theta,0,B\sin\theta)$ applied at an angle θ to the normal to the well walls (see Fig. 1). The magnetic field was represented by the vector potential $\mathbf{A}=(0,Bx\sin\theta-Bz\cos\theta,0)$, for which the Hamiltonian is invariant under translations along the y direction. In this gauge, the electron dynamics in the well reduce to two-dimensional $(x\text{-}z)$ motion described by the Hamiltonian,[33]

$$H=\frac{p_x^2+e^2B^2(x\sin\theta-z\cos\theta)^2+p_z^2}{2m^*}-eFx. \qquad (1)$$

In Eq. (1), the origin of the x coordinate is at the center of the well, p_x, p_z are momentum components, and m^* is the effective mass of an electron in the QW. We include the effects of conduction-band nonparabolicity in our model. In particular, we measure the energy dependence of m^* by studying the resonances in the experimental $I(V)$ plots for $B=0$.[37,40] Between collisions with the barriers, the orbital paths in the $x\text{-}z$ plane can be determined analytically for all θ.[32,33,35,44] Successive orbital segments are linked by specular reflection from the well walls. We have used Poincaré sections (slices through the classical phase space[1]) to investigate how the tilted magnetic field affects the electron dynamics. Figures 3(a)–3(c) show Poincaré sections for particular sets of the experimental parameters V, B, and θ. The sections are constructed from orbits with a range of starting velocities at the LH side of the well consistent with the energy of electrons tunneling from the 2DEG. In each plot, the scattered points show the lateral velocity components (v_y,v_z) every time the electron hits the LH (emitter) barrier. When $V=480$ mV, $B=12$ T, and $\theta=0°$, the electrons in the QW follow helical paths around the magnetic-field axis and collide with the two confining barriers in turn. These orbits are stable and produce a circular island (comprising a series of rings) in the Poincaré section [Fig. 3(a)]. When the magnetic field is tilted at 30° to the normal to the well walls [Fig. 3(b)], an island of stable regular motion persists towards the LH side of the Poincaré section, but it is embedded in a sea of chaos. The size of the chaotic sea increases with the magnetic-field strength and fills the phase space when $B=42$ T [Fig. 3(c)]. The regime of strong classical chaos has been explored in tunneling spectroscopy experiments on a range of RTDs[32,33,36,37] and is now well understood. Here, we consider how the mixed stable-chaotic dynamics that characterize the transition to chaos affect the quantized states and tunneling characteristics of the RTD. The islands of stability in a mixed phase space can be classified by considering the periodic orbits at the center of the each island. Henceforth, we refer to a periodic trajectory in which the electron makes, respectively, l and r collisions with the LH and right-hand (RH) barrier per period as an (l,r) orbit. The almost circular stable island in Fig. 3(b) contains remnants of the helical traversing orbits that fill the phase space when $\theta=0°$ [Fig. 3(a)]. At the center of this island there is a (1,1) stable orbit [top diagram in Fig. 3(d)] in which the electron completes one return journey across the QW per period. Away from the center, there is a three-fold splitting or period-tripling bifurcation that creates the three crescent-shaped islands shown in Fig. 3(b) and (enlarged) in Fig. 3(e). The successive breakdown of large stable islands into smaller island chains drives the transition to chaos in this system.[35,44] The period-tripling bifurcation shown in

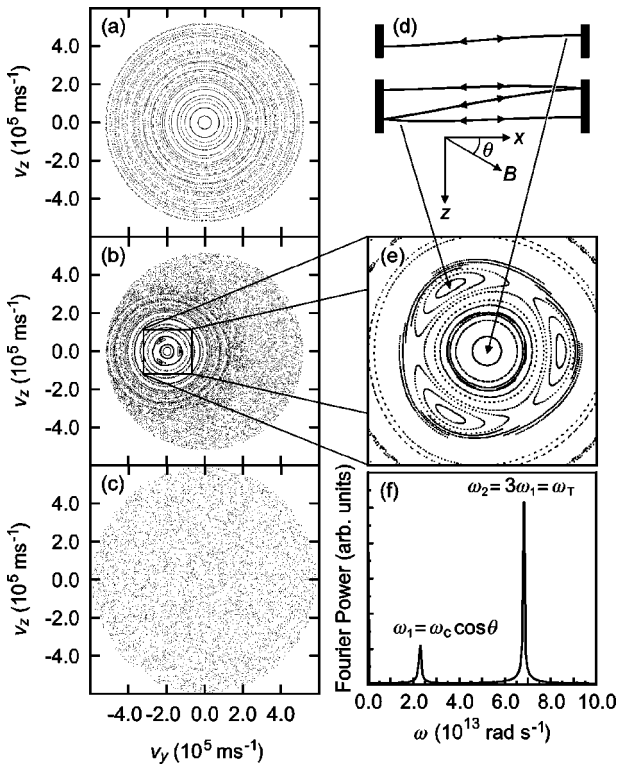

FIG. 3. Poincaré sections calculated at the energy of electrons entering the QW for $V=480$ mV, and $\theta=0°$, $B=12$ T (a); $\theta=30°$, $B=12$ T (b); $\theta=30°$, $B=42$ T (c). The scattered points show the lateral velocity components (v_y, v_z) for collisions on the LH barrier corresponding to electron orbits with a range of initial velocities for fixed total energy. Upper [lower] diagrams in (d) show (1,1) [(3,3)] stable periodic orbits projected on x-z plane (axes and magnetic-field orientation inset). These orbits lie at the center of the circular [three crescent-shaped] stable island(s) in (b), which are shown enlarged in (e). The Fourier power spectrum (f) of $x(t)+z(t)$ for the (3,3) stable periodic orbit reveals two distinct frequencies ω_1 and $\omega_2=3\omega_1$.

Figs. 3(b) and 3(e) creates a (3,3) stable orbit, located at the centers of the three crescent-shaped islands, in which the electron completes three return trips across the QW before closing the path [lower diagram in Fig. 3(d)].

Stable orbits are always separable in some coordinate system.[61] Since the Hamiltonian for the system reduces to two-dimensional motion in the x-z plane,[33] the theory of action-angle variables[61] tells us that it is always possible to define a transformation from x and z to new coordinates α and β in which the motion is separable. In the new coordinate system, the electron orbit lies on the surface of a torus, and the position of the electron at time t is specified by angles $\alpha(t)$ and $\beta(t)$ around the neck and circumference of the torus. The corresponding angular frequencies $\omega_1 = d\alpha/dt$ and $\omega_2 = d\beta/dt$ are constants of the motion that depend on the shape of the orbit. These frequencies can be obtained by Fourier transforming the sum of the x and z coordinates of the electron orbits plotted as a function of t.[34] The Fourier power spectrum in Fig. 3(f) shows that for the (3,3) stable orbit, ω_1 equals the cyclotron frequency $\omega_c \cos\theta = eB\cos\theta/m^*$, corresponding to the magnetic-field component perpendicular to the well walls. The second frequency ω_2 is exactly three times larger and equals the angular frequency ω_T (defined above) for the one-dimensional motion across the QW that an injected electron would perform in zero magnetic field. Similar results are obtained for all orbits within the stable islands shown in Fig. 3. It is because $\omega_2=3\omega_1$ for these orbits that the period-tripling bifurcation shown in Fig. 3(e) occurs and produces the stable islands around the (3,3) periodic orbit. The period-tripling bifurcation is a consequence of resonance[61] between the two characteristic frequencies of the stable (1,1) periodic orbit, which splits the phase space surrounding this orbit into a chain of three crescent-shaped islands [shown in Fig. 3(e)].

Although the QW is sufficiently narrow for each of its box-quantized energy levels (associated with one-dimensional motion along the x direction) to produce a well-resolved resonant peak in the experimental $I(V)$ curve at $\theta=0°$ (Fig. 2), it is also wide enough to support many quasi-bound states (approximately 20–30 when $\theta=30°$). This enables us to relate the quantized states to the corresponding classical phase space. To explore this relation, we calculated the QW eigenstates using a matrix diagonalization method[33,40] and taking the same magnetic vector potential as for the classical analysis. In this gauge, the y dependence of the wave functions is a plane wave, and so the probability density of the eigenstates depends only on the x and z coordinates.[33] When $\theta=0°$, the electron motion along the x and z directions is separable, and the total energy of the electron, ε, is given by the energy-level spectrum of the box-quantized states for one-dimensional motion across the QW (x direction), plus Landau levels corresponding to motion parallel to the well walls. In a semiclassical picture,[34] the spacing of adjacent one-dimensional box-quantized states equals $\hbar\omega_T$, where ω_T is the angular frequency corresponding to a single return trip across the QW. We used a transfer-Hamiltonian approach[33] to calculate the rates of tunneling transitions from the single (lowest energy) occupied Landau level in the emitter 2DEG, into the quantized states of the QW. These transition rates were then used to obtain theoretical current-voltage $I(V)$ characteristics for the RTD. Figure 4(a) shows the $I(V)$ curve calculated for $B=12$ T and $\theta=0°$, using an energy-dependent effective mass m^* defined previously[37] to account for conduction-band nonparabolicity. The curve contains a series of resonant peaks, and the insets show probability-density plots for the emitter and well-state wave functions at each resonance. Due to the conservation of angular momentum, the electrons can only tunnel into the lowest Landau states in the QW, which have nonzero overlap integrals with the occupied emitter state. The resonant peaks in $I(V)$, therefore, originate from transitions into successive one-dimensional box-quantized states of the QW. In our theory, the electric field F in the QW is assumed to be proportional to the applied bias voltage. The validity of this constant-capacitance approximation has been demonstrated previously for a wide range of resonant tunneling structures.[36,37] Here, the scaling factor $\gamma=F/V$ was determined by fitting the positions of the resonant peaks calculated for $\theta=0°$ to the corresponding experimental data shown in Fig. 4(b), from which we subtracted a smooth

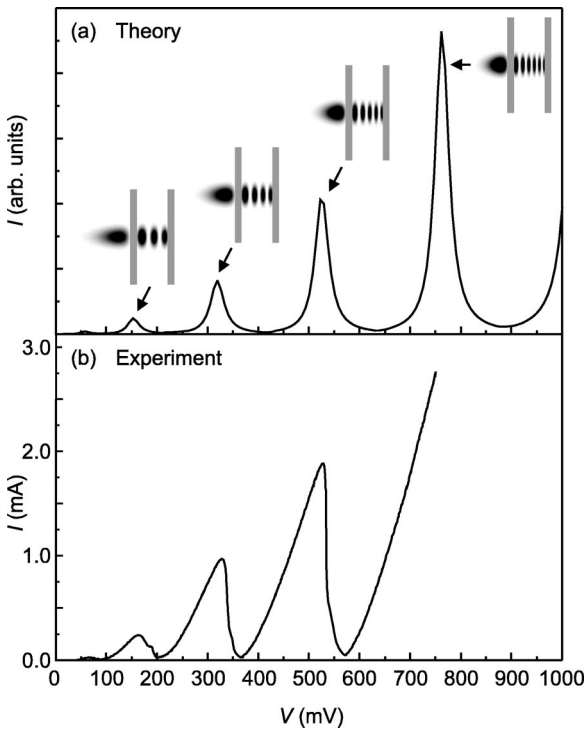

FIG. 4. $I(V)$ curves calculated (a) and measured (b) for the RTD with $\theta=0°$ and $B=12$ T. A smooth monotonic background has been subtracted from the experimental data to emphasize the resonant peaks. Insets in (a) show probability density plots in the x-z plane (white = 0, black = high) of the emitter and well state wave functions at each arrowed resonance. Gray rectangles show positions of the barriers. $I(V)$ curve (b) was only measured for $V \leqslant 750$ mV to avoid overheating the sample.

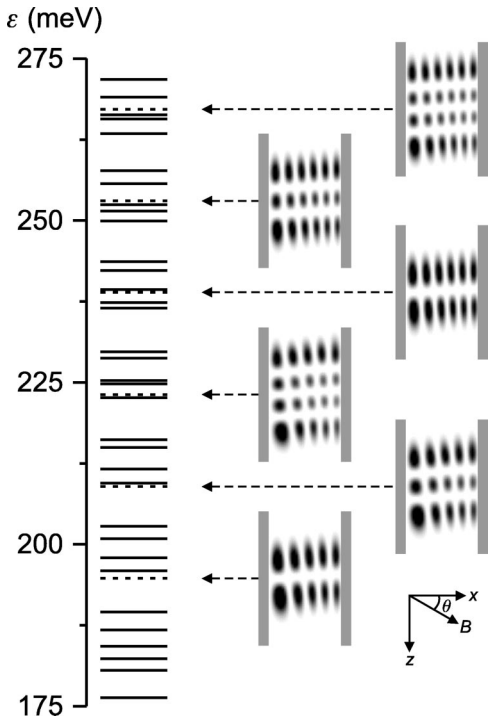

FIG. 5. Energy levels of the QW calculated for $B=12$ T, $\theta=30°$, and $V=630$ mV. For these parameters, the total energy of electrons tunneling into the well is $\varepsilon=195$ meV. RH gray-scale plots show probability density (white = 0, black = high) in x-z plane (axes and magnetic field orientation inset) of eigenstates corresponding to quasi-Landau levels (dashed lines). Gray rectangles show positions of the barriers.

monotonic background in order to emphasize the resonant structure. The good agreement between the positions of resonant peaks in the calculated and measured $I(V)$ curves at $\theta=0°$ shows that the constant-capacitance approximation is accurate for a wide range of bias voltages.

We now consider the eigenstates of the QW taking parameters $V=630$ mV, $\theta=30°$, and $B=12$ T that produce a mixed stable chaotic phase space at the electron injection energy, containing a period-tripling bifurcation like that shown for lower V in Figs. 3(b) and 3(e). Since a large chaotic sea surrounds the stable islands, the corresponding eigenvalues of the total electron energy have a highly irregular spectrum. This can be seen from Fig. 5, which shows a sequence of energy levels close to the electron injection energy (195 meV). Most of the associated eigenfunctions are either scarred by unstable periodic orbits or have highly irregular and diffuse spatial patterns.[40] Despite this complexity, there is a subset of equally spaced energy levels (dashed lines in Fig. 5), which originate from quantizing the classical orbits within the stable islands shown in Figs. 3(b) and 3(e). Semiclassical quantization of the two separable variables α and β (defined above) associated with each of these stable orbits produces two independent level ladders that add to give the total energy of the electron. The spacing of neighboring energy levels associated with variable α (β) is $\hbar\omega_1$ ($\hbar\omega_2$). Since $\omega_2 \simeq 3\omega_1$ for orbits within all of the stable islands shown in Figs. 3(b) and 3(e), the corresponding total energy eigenvalues are quasi-Landau levels that are equally spaced by $\hbar eB\cos\theta/m^*$. As shown in Fig. 5, these quasi-Landau levels (dashed lines) are embedded within the full energy-level spectrum for the QW. The probability-density plots of the associated eigenfunctions are also shown in Fig. 5. They exhibit regular antinode patterns that resemble the simple Landau and one-dimensional box-quantized states found for $\theta=0°$ [see insets in Fig. 4(a)]. For example, the three probability-density plots in the bottom half of Fig. 5 all have five antinodes across the well and correspond to the 5th box-quantized state of the well when $\theta=0°$. They form a triplet of successive quasi-Landau states with two, three, and four lateral antinodes. The three probability distributions in the top half of Fig. 5 correspond to the same sequence of Landau states, but have six antinodes for motion across the well.

We now consider how the quantized states of the QW manifest themselves in the tunneling characteristics of the RTD. Figure 6 shows theoretical (a) and experimental (b) $I(V)$ curves for $\theta=30°$ and $B=12$ T. These magnetic-field parameters produce a mixed stable-chaotic phase space at the electron injection energy for all of the voltages shown in Fig. 6. A smooth monotonic background has been subtracted from the measured curve in Fig. 6(b) to emphasize the resonant peaks. The filled black (gray) arrows in Fig. 6(a) indicate two distinct series of periodic resonant peaks in the calculated $I(V)$ curve. These peaks have a voltage spacing of

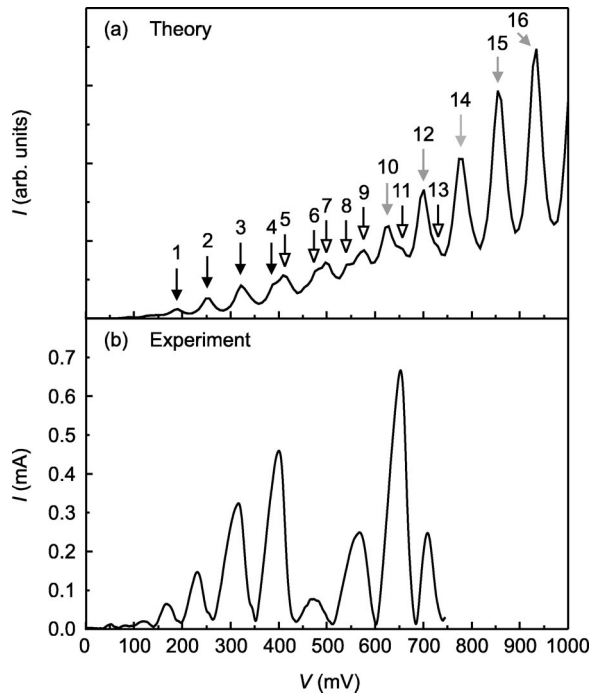

FIG. 6. $I(V)$ curves calculated (a) and measured (b) for the RTD with $\theta=30°$ and $B=12$ T. (a) Positions of (numbered) resonant peaks associated with the following: black arrow heads, unstable (1,2) orbits; white arrow heads, unstable (1,2), stable (1,1), and stable (3,3) orbits; gray arrow heads, stable (1,1) and stable (3,3) orbits. $I(V)$ curve (b) was only measured for $V\leqslant 750$ mV to avoid overheating the sample.

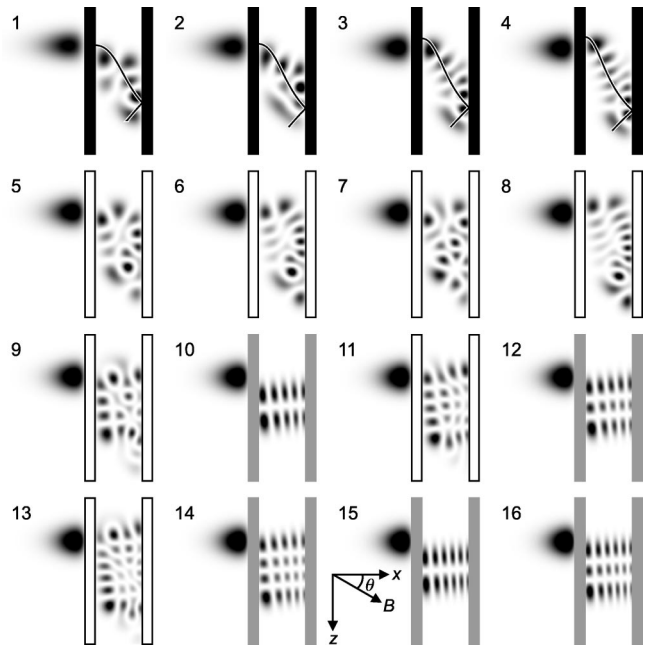

FIG. 7. Probability-density plots (white = 0, black = high) in x-z plane (axes inset) of the emitter and well state wave functions corresponding to each numbered resonance in Fig. 6(a). Rectangles filled black, white, and gray show positions of barriers for wave functions associated with unstable (1,2); unstable (1,2), stable (1,1), and stable (3,3); stable (1,1) and stable (3,3) orbits, respectively. Curves in top row show paths of unstable periodic (1,2) orbits, projected onto x-z plane, which scar the wavefunctions on which they are superimposed.

‘~ 74 mV, which is similar to the value of ~ 77 mV for the corresponding resonant structure observed in the experimental data, and approximately three times smaller than for $\theta=0°$ (Fig. 4). The theoretical $I(V)$ curve also contains a series of weaker and less evenly spaced resonant features which are marked by arrows with open white heads in Fig. 6(a).

Figure 7 shows probability-density plots for the single occupied emitter state (to the left of the two rectangles representing the barriers) and the individual well states $\psi_n(x,z)$ that generate each of the (numbered) resonant features in the calculated $I(V)$ curve [Fig. 6(a)]. The subscript n relates each eigenfunction to a particular numbered resonant peak in Fig. 6(a). We now consider the structure of the wave functions, and their relation to the classical motion of electrons in the well. The four QW wave functions in the top row of Fig. 7 are scarred by the (1,2) unstable periodic orbits shown overlaid. The scarring occurs whenever the classical action for the orbit $S=(j+\phi)h$, where $\phi\sim 1.2$ is a constant phase factor and j is the number of antinodes in the scar pattern along the classical path.[33] Wave functions 1–4 in Fig. 7 form a sequence of scarred states with $j=5-8$. Quantization of the classical action means that for given V, the energy spacing of adjacent QW states scarred by the (1,2) orbit is $\hbar\omega_{(1,2)}$, where $\omega_{(1,2)}\sim\omega_T/3$ is the angular frequency for the periodic motion. This spacing is approximately three times smaller than that of the box-quantized states of the well at $\theta=0°$. To link each of the quantized well states in Fig. 7 to the corresponding classical phase space, we have calculated the Wigner functions[62] defined by

$$W_n(x,z,v_x,v_z)=\frac{1}{h^2}\int_{-\infty}^{\infty}\int_{-\infty}^{\infty}\psi_n^*\left(x+\frac{\lambda_x}{2},z+\frac{\lambda_z}{2}\right)\times\psi_n\left(x-\frac{\lambda_x}{2},z-\frac{\lambda_z}{2}\right)\times\exp[-im^*(v_x\lambda_x+v_z\lambda_z)/\hbar]d\lambda_x d\lambda_z, \tag{2}$$

where λ_x and λ_z are real variables. We transformed W_n to a two-dimensional function of v_y and v_z in the following way. First, in Eq. (2), we set $x=-w/2$, so that the Wigner function is calculated at the LH side of the QW, just like the classical Poincaré sections shown in Figs. 3 and 9. For this value of x and specified velocity components (v_y,v_z), $z=x\tan\theta-m^*v_y/eB\cos\theta$,[40] and v_x is obtained from the total energy ε, and the form of the Hamiltonian, Eq. (1), for two-dimensional (x,z) motion in the QW. Figure 8 shows W_n as a function of v_y and v_z for $n=1,2,3,\ldots,16$. The Wigner functions reveal the distribution of lateral velocity components (v_y,v_z) for each eigenfunction and are quantum analogues[62] of the classical Poincaré sections shown in Fig. 9, in which (v_y,v_z) are plotted each time the electron collides with the LH barrier. These Poincaré sections are calcu-

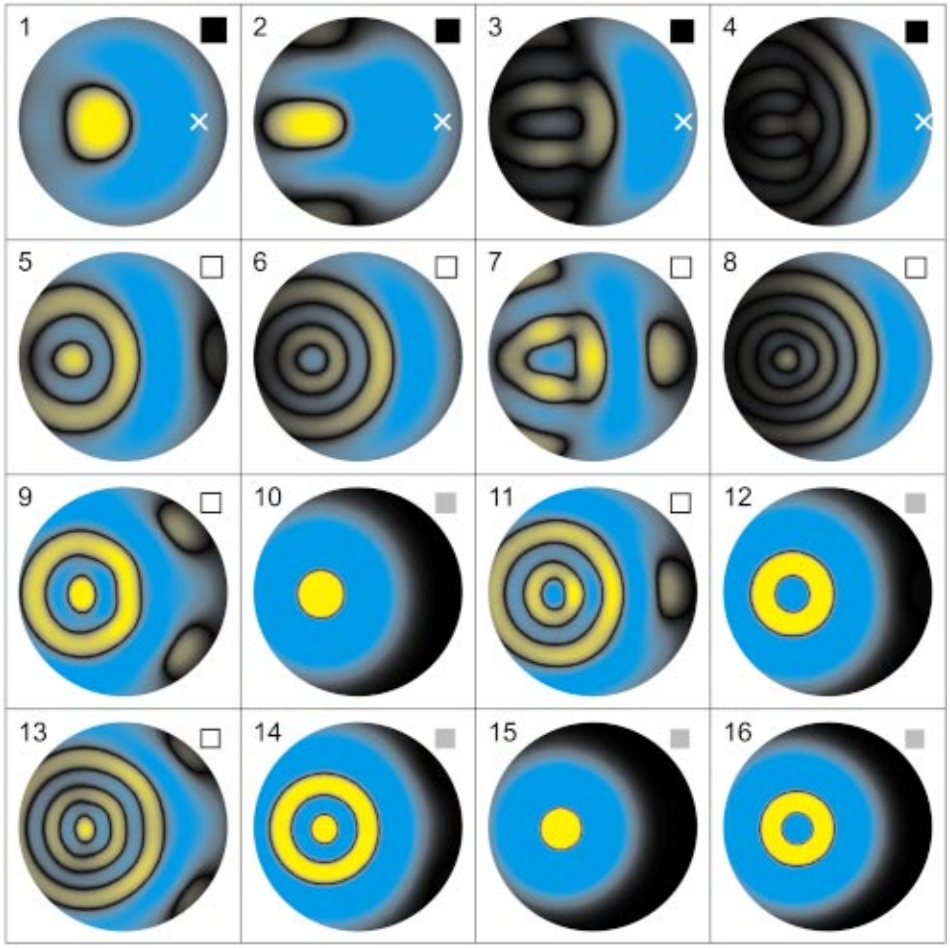

FIG. 8. (Color) Wigner functions (blue >0, yellow <0, black $=0$) calculated for the well state wave functions with probability distributions shown in Fig. 7, and corresponding to the numbered resonant features in Fig. 6(a). Squares filled black, white, and gray at top right of each plot all have a sidelength of 10^5 ms^{-1}. They indicate scale of Wigner functions associated with unstable (1,2); unstable (1,2), stable (1,1), and stable (3,3); and stable (1,1) and stable (3,3) orbits, respectively. Crosses in plots 1–4 mark starting velocities (v_{y0},v_{z0}) for the (1,2) unstable periodic orbits shown in plots 1–4 of Fig. 7. The origin of each plot is at the center of the surrounding square frame.

lated for voltages corresponding to each of the numbered resonant peaks shown in Fig. 6(a), at the energy of electrons entering the QW. In the top RH corner of each plot in Figs. 8 and 9, there is a square of sidelength 10^5 ms^{-1}, which indicates the scale. Comparison of Figs. 8 and 9 shows that the form of the Wigner functions reflects the structure of the classical phase space. In particular, the stable islands at the LH sides of the Poincaré sections appear as ringlike patterns in the Wigner functions (for example, compare plots 10, 12, and 14–16 of Figs. 8 and 9). More subtle features of the Poincaré sections are also reproduced by the Wigner functions. For example, the period-tripling bifurcation revealed by Poincaré section number 7 of Fig. 9 appears as a chain of three yellow islands in the corresponding Wigner function (Fig. 8). The period-doubling bifurcation in Poincaré sections 1–3 of Fig. 9 also manifests itself in the associated Wigner functions. This is most easily seen in Wigner function 2 where two blue arms extend towards the left and pass right through the upper and lower islands of stability in the classical phase space. In addition, just to the right of the circular island in Poincaré section 4 of Fig. 9, there is a small crescent-shaped stable island produced by (1,3) stable orbits (previously called type-3 stable orbits[34,39]). This island appears as a yellow crescent in the corresponding Wigner function.

Even though the (1,2) unstable periodic orbits that scar wave functions 1–4 in Fig. 7 have zero measure in the classical phase space, they show up clearly in the corresponding Wigner functions (Fig. 8). In particular, the Wigner functions have large positive values (blue islands in plots 1–4 of Fig. 8) near the starting velocities (v_{y0},v_{z0}) of the (1,2) unstable periodic orbits (crosses in Fig. 8). Note that the starting velocities of the (1,2) orbits lie to the right of the blue islands in the Wigner functions, rather than at the center of the islands. This is partly because the energies and quantum numbers of the scarred states are too low (not close enough to the semiclassical limit) to give precise quantitative agreement with the corresponding classical phase space, and partly because the quantum states are calculated for $(Al_{0.4}Ga_{0.6})As$ barriers of finite height (to obtain a nonzero tunnel current), whereas the classical orbits are enclosed by impenetrable barriers.

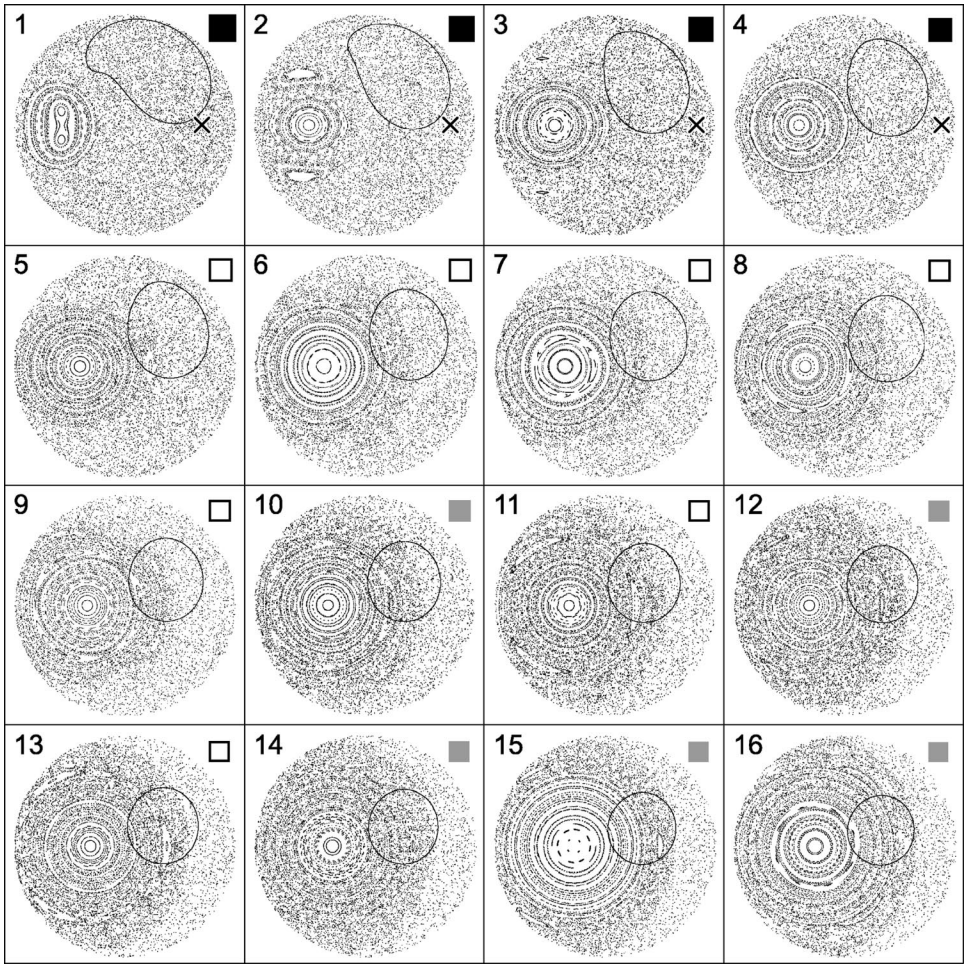

FIG. 9. Poincaré sections calculated at the energy of electrons entering the QW for voltages corresponding to the numbered resonant peaks in Fig. 6(a). The scattered points show the lateral velocity components (v_y, v_z) for collisions on the LH barrier corresponding to classical orbits with a range of initial conditions consistent with the electron injection energy. Squares filled black, white, and gray at top right of each plot all have a sidelength of 10^5 ms^{-1}. They indicate scales of Poincaré sections associated with unstable (1,2); unstable (1,2), stable (1,1), and stable (3,3); and stable (1,1) and stable (3,3) orbits, respectively. Crosses in plots 1-4 mark starting velocities (v_{y0}, v_{z0}) for the (1,2) unstable periodic orbits shown in plots 1–4 of Fig. 7. Solid continuous curves show approximate range of lateral starting velocities for electrons tunneling into the QW. The origin of each plot is at the center of the surrounding square frame.

IV. INTERPRETATION OF EXPERIMENTS IN A TILTED MAGNETIC FIELD

We now use Figs. 7 –9 to explain the origin of the resonant peaks in the theoretical $I(V)$ curve [Fig. 6(a)] and corresponding experimental data [Fig. 6(b)]. First we consider the peaks numbered 1–4 in Fig. 6(a), which originate from tunneling into the scarred states shown in plots 1–4 of Fig. 7. As noted above, for given V, the energy spacing of adjacent scarred states in the well is $\sim \hbar \omega_T/3$, that is approximately three times smaller than for the box-quantized states of the well at $\theta = 0°$. Consequently, as V is changed so that the bound-state energy of the emitter 2DEG scans the level spectrum of the QW, we expect that resonant tunneling into these scarred states will generate a regular series of resonant peaks in $I(V)$, with a voltage spacing ~ 3 times smaller than for $\theta = 0°$. The amplitudes of the resonant peaks depend on the tunneling matrix elements, which are determined by the overlap between the emitter and well-state wave functions. The LH antinode of each scarred wave function in Fig. 7 is closely aligned with the single occupied (lowest energy) Landau state in the emitter 2DEG, whose probability distribution is shown by the antinode to the left of the potential barriers. Tunneling transitions from the emitter into the scarred states of the QW, therefore, have large matrix elements,[37] and generate the evenly-spaced peaks 1–4 in the calculated $I(V)$ curve [Fig. 6(a)]. The large tunneling matrix elements are a consequence of momentum conservation in a classical picture. Electrons launched from the 2DEG enter the QW approximately within the regions of (v_y, v_z) phase space enclosed by the solid continuous closed curves in Fig. 9. The positions and shapes of these regions (which are approximately circular for plots 13–16) were estimated by calculating the classical momentum transferred as the electrons move from the 2DEG to the LH edge of the QW.[32,34] In plots 1–4 of Fig. 9, the ranges of lateral velocities for electrons entering the well are very close to the starting velocities (v_{y0}, v_{z0}) of the (1,2) unstable periodic orbits, which are marked with crosses. This type of orbit is, therefore, directly

accessible to the tunneling electrons. It has been detected previously in our experiments on RTDs containing either a 120 nm[32,40] or 22 nm[37] wide QW, but in these previous studies the accessible phase space was strongly chaotic. For the present device, tunneling transitions into states scarred by (1,2) unstable periodic orbits generate the resonant peaks observed in the experimental data for $V \lesssim 400$ mV. Comparison of Figs. 6(a) and 6(b) reveals that the voltage positions and spacings of these peaks are in good quantitative agreement with the theory.

Resonant peaks 10, 12, 14, 15, and 16 marked by gray arrows in Fig. 6(a) originate from tunneling transitions from the 2DEG into the quasi-Landau states shown in Fig. 5 and numbered 10, 12, 14, 15, and 16 in Fig. 7. The corresponding Wigner functions contain striking ring patterns concentrated within the islands of stability in the classical phase space (Fig. 9). The total number of rings (yellow and blue) in each Wigner function equals the number of lateral antinodes in the corresponding probability-density plots. Although these quasi-Landau states have different numbers of lateral antinodes, they all contribute to the tunnel current because, in contrast to $\theta = 0°$, the Landau level index is not conserved in tunneling transitions from the single occupied Landau level in the emitter 2DEG. This is because, in a quantum picture, the tilted magnetic field produces a relative shift of the emitter and well-state wave functions along the z axis. As shown in Fig. 7, this aligns antinodes of the emitter and well states, thereby producing large tunneling matrix elements. This displacement of the emitter and well state wave functions corresponds to the classical momentum transferred by the Lorentz force as the electrons move from the 2DEG to the QW. For $V \gtrsim 550$ mV, the distribution of initial velocities for electrons entering the QW (solid curves in Fig. 9) intersects the stable islands associated with the period-tripling bifurcation (see plots 8–16 in Fig. 9). Stable orbits within these islands are, therefore, accessible in energy and momentum-conserving transitions from the emitter 2DEG. In previous experiments on wider QWs,[36] these orbits were not accessible in energy- and momentum-conserving transitions from the 2DEG.[39] This is because for given V, ω_T is lower for the wider wells, and so the period-tripling bifurcation for which $\omega_T = 3\omega_c \cos\theta$ occurs at lower magnetic fields. As a consequence, the in-plane (z) component of magnetic field is too small to bend the electron trajectories sufficiently for them to enter the QW within the stable islands around the bifurcation. The peak tripling observed in the previous experiments[36] actually originates from transitions into stable (1,3) orbits in a different part of the phase space.[39,40]

Note that Wigner functions 10, 12, 14, 15, and 16 in Fig. 8 fill all of the phase space occupied by stable islands in the Poincaré sections, rather than being concentrated within the stable islands corresponding to just the (1,1) orbits or just the (3,3) orbits. We, therefore, conclude that the quasi-Landau states originate from quantizing both the (1,1) and (3,3) orbits, and so the contributions of those orbits to the tunnel current cannot be distinguished. Since $\omega_1 = \omega_T/3$ for all of these orbits, the voltage spacing of the resonant peaks is approximately three times smaller than for $\theta = 0°$ in both the calculated [Fig. 6(a)] and measured [Fig. 6(b)] $I(V)$ curves. A detailed analysis of inter-Landau-level transitions for electrons in a RTD with a narrow (~ 10 nm) QW and a small (~ 5 T) tilted magnetic field has been reported previously.[57] In these calculations, the magnetic-field component in the plane of the QW was treated as a perturbation, which allowed analytical expressions for the tunneling rates to be obtained. This approximation is invalid for states associated with the chaotic part of the phase space where there is strong mixing of motion along the x and z directions. But it works well for the subset of quasi-Landau states whose structure is primarily determined by the magnetic-field component perpendicular to the well walls, and corresponds to stable orbits within the chaotic sea.

Next we consider resonant peaks 5–9, 11, and 13 [marked by arrows with white heads in Fig. 6(a)], which occur in the voltage range 400 mV $\lesssim V \lesssim$ 725 mV. The wave functions and Wigner functions corresponding to these peaks have a mixed stable-chaotic character and contain features associated with (1,1) and (3,3) stable orbits, plus (1,2) unstable periodic orbits. In particular, the Wigner functions have nonzero amplitudes throughout both the regular and chaotic parts of the corresponding classical phase space. As the peak index increases, the probability-density plots for these hybrid stable-chaotic states gradually become more regular, reflecting the transition from peaks 1–4 associated with (1,2) unstable orbits to peaks 10, 12, and 14–16 associated with stable orbits. For example, the wave functions with high indices 9, 11, and 13 in Fig. 7 form a sequence of states with fairly regular probability distributions comprising four antinodes across the well, and respectively four, five, and six lateral antinodes. The resonant peaks corresponding to these three states have approximately equal voltage spacings in Fig. 6(a). Since all of the hybrid stable-chaotic states originate from complex quantum interference processes associated with more than one type of classical path, their energy spacings are not constant. Consequently, the voltage spacings of the corresponding resonant peaks in the calculated $I(V)$ curve [marked by arrows with white heads in Fig. 6(a)] are not generally regular. Since the Wigner functions for the hybrid states extend across the whole (v_y, v_z) phase space, these states couple less strongly to the emitter 2DEG than the scarred or quasi-Landau states in Figs. 7 and 8, whose Wigner functions are concentrated near the starting velocities for electrons entering the QW. This explains why, in the calculated $I(V)$ curve [Fig. 6(a)], the resonant peaks due to transitions into the hybrid stable-chaotic states in the range 400 mV $\lesssim V \lesssim$ 725 mV generally have lower amplitudes than peaks outside this voltage range, which are associated with either purely stable or purely unstable classical paths. We observe a broadly similar region of diminished oscillatory amplitudes in the experimental data [12 T trace in Fig. 2 and Fig. 6(b)]. The voltage dependence of the calculated peak heights is in reasonable qualitative agreement with the data, particularly for $V \lesssim 400$ mV. Precise quantitative agreement between the measured and calculated peak heights is, however, lacking for three reasons. First, a smooth monotonic background has been subtracted from the experimental $I(V)$ curve in Fig. 6(b) in order to emphasize the resonant peaks. The heights of these peaks are, therefore, not directly

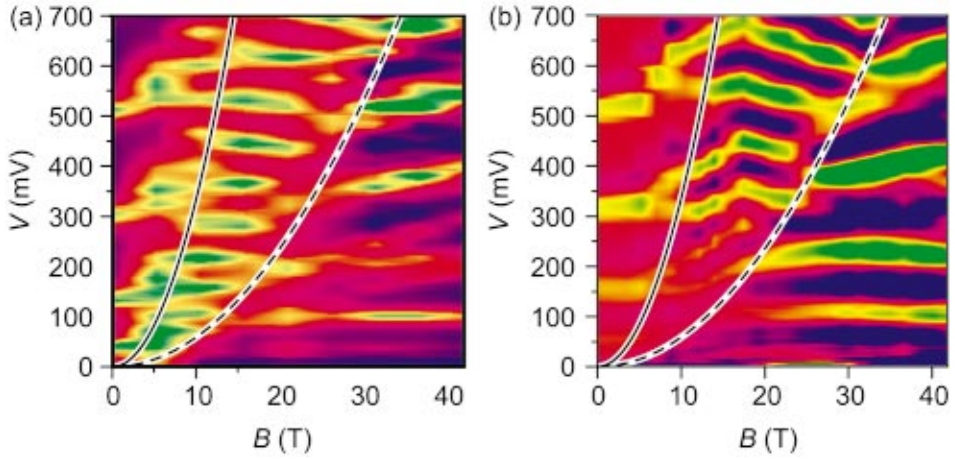

FIG. 10. (Color). Contour plots plots (green = high, blue = low) of I versus B and V calculated (a) and measured (b) for the RTD with $\theta = 30°$. The plots are constructed from $I(V)$ curves calculated or measured for a range of B values, with smooth backgrounds subtracted to emphasize the resonant peaks. Solid parabolas show locus of B and V values where $\omega_T = 3\omega_c \cos\theta$ for electrons injected into the QW. Within the region of B-V space between the solid and dashed parabolas, the voltage spacing of adjacent resonant peaks is approximately three times smaller than at $B = 0$. To the right of the dashed parabolas, the voltage spacings of adjacent resonant peaks are comparable with the values observed for $B = 0$.

comparable with those in the calculated $I(V)$ curve [Fig. 6(a)], from which no background has been subtracted. Second, the tunnel current is exponentially sensitive to the barrier parameters: thickness, potential height, and effective mass. Uncertainties in these parameters for an actual experimental device, therefore, make it hard to predict the exact magnitude of the current. We estimate these uncertainties to be approximately ± 1 atomic monolayer in the tunnel barrier thickness, $\pm 5\%$ in the potential height of the barrier, and approximately $\pm 10\%$ in the tunneling effective mass. Third, the calculated peak heights depend on several approximations made in our theoretical analysis, which is based on the transfer-Hamiltonian formalism for tunneling through high and wide barriers.[33] Within this formalism, the tunnel current into each QW state is proportional to the square of the transition matrix element, which is determined by the amplitudes of the emitter and QW wave functions in the LH barrier, and also depends on the energy-level lineshape. To estimate the level broadening, we assumed that the scattering rate of electrons in the QW equals the longitudinal optic-phonon emission rate in bulk GaAs. But the QW wave functions, which determine the scattering rate, are completely different from those of bulk GaAs and can change dramatically from one QW level to the next. Also, atomic monolayer fluctuations in the thickness of the barriers and the QW are likely to affect the linewidths. Consquently, each QW state might have its own characteristic energy broadening and line shape. This would affect the relative heights of the peaks in $I(V)$ and explain why weaker resonant features and shoulders in the theoretical $I(V)$ curve, Fig. 6(a), are not observed in the corresponding experimental data. In our calculation of the matrix elements for tunneling transitions from the emitter 2DEG into the QW, we assumed that the emitter wave function is separable, that the electronic effective mass is independent of position in the QW and also independent of energy in the barriers. Since the transition rate is exponentially sensitive to the effective mass,[33] as well as to the uncertainties in the barrier thickness and height, it is difficult to make accurate calculations of the current magnitude. For these reasons, we have not specified the current scale in Fig. 6(a).

We have investigated how the $I(V)$ characteristics of the RTD change with magnetic field at a fixed tilt angle of 30°. Figure 10 shows color contour plots of the current calculated (a) and measured (b) as a function of V and B. To emphasize the resonant peaks in this type of contour plot, it was necessary to subtract a smooth background from all of the theoretical and experimental $I(V)$ curves (some of which are shown in Fig. 2) used to construct Fig. 10. The experimental and theoretical plots both reveal similar features, which we now consider in detail. The solid curves in Fig. 10 both show the locus of B and V values for which the resonance condition $\omega_T = 3\omega_c \cos\theta$ is satisfied. Since $\omega_T \propto V^{1/2}$,[59] and $\omega_c \propto B$, this locus forms a parabola in B-V space. To the left of this parabola, the simulated contour plot of $I(V,B)$ [Fig. 10(a)] contains only widely spaced resonant peaks ($\Delta V \simeq 200$ mV for $V \simeq 400$ mV), which appear as a series of yellow/green bands. These peaks originate from resonant tunneling into the one-dimensional box-quantized states of the QW that are only weakly perturbed by a small tilted magnetic field. Just to the right of the boundary in the calculated color contour plot [Fig. 10(a)], the number of resonant peaks (yellow/green bands) within a given voltage interval suddenly triples. This is because when $\omega_T \simeq 3\omega_c \cos\theta$, the QW supports a sequence of accessible Landau-like states similar to those shown in Figs. 5 and 7. Tunneling transitions into these states produce strong resonant peaks [for example, peaks 10, 12, 14, 15, and 16 in Fig. 6(a)] with a voltage spacing three times smaller than for $\theta = 0°$. A changeover to resonances with voltage spacings reduced by a factor of ~ 3 also occurs in the experimental data [Fig. 10(b)], along the solid parabolic boundary in B-V space. Note that the Landau-like states only generate large peaks in $I(V)$ for B and V values which are close to the solid

parabolic boundaries in Fig. 10. In the region of B-V space between the solid and dashed parabolas, the electrons tunnel mainly into (1,2) unstable periodic orbits that, as shown on Fig. 7, scar subsets of eigenstates and thereby generate periodic resonant peaks in $I(V)$. Since the period of these orbits is roughly three times longer than the traversing orbits found for $\theta=0°$, the voltage spacing of the associated resonant peaks is approximately three times smaller than for $\theta=0°$, just as for the resonances associated with quasi-Landau states. For large magnetic fields to the right of the dashed parabolic boundaries in Fig. 10, the voltage spacings of the resonant peaks in both the calculated and measured $I(V,B)$ color contour plots suddenly increase and approach values close to those observed for $\theta=0°$. In this high B regime, the resonant peaks appear as a series of yellow/green bands in the experimental data, and either yellow/green or red bands in the theory. Similar behavior has been observed previously,[36] and occurs because the electrons tunnel into unstable but periodic traversing orbits whose periods are very similar to the traversing orbits found for $\theta=0°$. Note that the current peaks evolve in a less regular way with increasing magnetic field in the experimental data [Fig. 10(b)] than in the theory [Fig. 10(a)]. This is primarily a consequence of noise in the experimental data, which is amplified by the background subtraction procedure used to construct the contour plot. Sample imperfections, such as charged impurities and monolayer fluctuations in the well and barrier widths, might also influence the positions of the resonant peaks in B-V space though, as noted in Sec. II, we used large spacer layers to minimize the diffusion of dopants into the QW and barrier regions.

V. CONCLUSION

In summary, we have investigated how period-tripling bifurcations of electron orbits in the QW of a RTD affect the corresponding quantized states and $I(V)$ characteristics of the device. The period-tripling bifurcations occur within an island of (1,1) stable orbits at B and V values for which the resonance condition $\omega_T \simeq 3\omega_c \cos\theta$ is satisfied. This condition defines a parabolic boundary in B-V space (solid curves in Fig. 10) along which the voltage spacing of the resonant peaks in both the calculated and measured $I(V)$ curves falls by a factor ~ 3. The resonant peaks close to this parabolic boundary originate from tunneling transitions into a series of quasi-Landau states whose energy spacing is three times smaller than that of the one-dimensional well states found for $\theta=0°$. By using Wigner functions to relate the eigenstates of the QW directly to the corresponding classical phase space, we have shown that the quasi-Landau states originate from the quantization of stable orbits close to the period-tripling bifurcation. The Wigner functions for the quasi-Landau states exhibit large amplitude fluctuations across the entire range of v_y and v_z values within the classical islands of stability. This demonstrates that the quasi-Landau states originate from quantization of both the traversing (1,1) and period-tripled (3,3) stable orbits. As V is reduced below the value required for the period-tripling bifurcation at a given B value, there is a changeover to resonant peaks associated with well states scarred by unstable periodic (1,2) orbits. Finally, we emphasize that despite the complex mixed stable-chaotic structure of the classical phase space, the tunneling process is dominated by small subsets of well states, which generate quasi-periodic resonant peaks in $I(V)$. These states are associated with both stable and unstable classical orbits within the small regions of phase space accessible to the tunneling electrons. Since particular periodic orbits control the tunneling rates, the $I(V)$ curves are insensitive to the universal statistical properties of the quantized states predicted by Random Matrix Theory.

ACKNOWLEDGMENTS

This work is supported by EPSRC (UK). L.E. thanks the University of Tokyo for a visiting professorship. R.K.H. was supported by the Royal Society.

[1] For reviews see: H.-J. Stöckmann, *Quantum Chaos — An Introduction* (Cambridge University Press, Cambridge, 1999); L. E. Reichl, *The Transition to Chaos* (Springer-Verlag, New York, 1992); M. C. Gutzwiller, *Chaos in Classical and Quantum Mechanics* (Springer-Verlag, New York, 1990).
[2] W. R. S. Garton and F. S. Tomkins, Astrophys. J. **158**, 839 (1969).
[3] A. Holle, J. Main, G. Wiebusch, H. Rottke, and K. H. Welge, Phys. Rev. Lett. **61**, 161 (1988).
[4] J. Main, G. Wiebusch, A. Holle, and K. H. Welge, Phys. Rev. Lett. **57**, 2789 (1986).
[5] R. V. Jensen, M. M. Sanders, M. Saraceno, and B. Sundaram, Phys. Rev. Lett. **63**, 2771 (1989).
[6] M. L. Du and J. B. Delos, Phys. Rev. A **38**, 1896 (1988); **38**, 1913 (1988).
[7] D. Wintgen and A. Hönig, Phys. Rev. Lett. **63**, 1467 (1989).
[8] D. Wintgen and H. Friedrich, Phys. Rev. A **36**, 131 (1987).
[9] H. Hasegawa, M. Robnik, and G. Wunner, Prog. Theor. Phys. Suppl. **98**, 198 (1989).
[10] F. L. Moore, J. C. Robinson, C. Bharucha, P. E. Williams, and M. G. Raizen, Phys. Rev. Lett. **73**, 2974 (1994).
[11] J. C. Robinson, C. Bharucha, F. L. Moore, R. Jahnke, G. A. Georgakis, Qian Niu, M. G. Raizen, and B. Sundaram, Phys. Rev. Lett. **74**, 3963 (1995).
[12] B. G. Klappauf, W. H. Oskay, D. A. Steck, and M. G. Raizen, Phys. Rev. Lett. **81**, 1203 (1998); **82**, 241 (1999).
[13] H. Ammann, R. Gray, I. Shvarchuck, and N. Christensen, Phys. Rev. Lett. **80**, 4111 (1998).
[14] W. H. Oskay, D. A. Steck, B. G. Klappauf, and M. G. Raizen, Laser Phys. **9**, 265 (1999).
[15] W. H. Oskay, D. A. Steck, V. Milner, B. G. Klappauf, and M. G. Raizen, Opt. Commun. **179**, 137 (2000).
[16] V. Milner, D. A. Steck, W. H. Oskay, and M. G. Raizen, Phys. Rev. E **61**, 7223 (2000).
[17] K. Vant, G. Ball, and N. Christensen, Phys. Rev. E **61**, 5994 (2000).

[18] M. El Ghafar, P. Törmä, V. Savichev, E. Mayr, A. Zeiler, and W. P. Schleich, Phys. Rev. Lett. **78**, 4181 (1997).
[19] K. Riedel, P. Törmä, V. Savichev, and W. P. Schleich, Phys. Rev. A **59**, 797 (1999).
[20] T. M. Fromhold, C. R. Tench, S. Bujkiewicz, P. B. Wilkinson, and F. W. Sheard, J. Opt. B: Quantum Semiclassical Opt. **2**, 628 (2000).
[21] C. M. Marcus, A. J. Rimberg, R. M. Westervelt, P. F. Hopkins, and A. C. Gossard, Phys. Rev. Lett. **69**, 506 (1992).
[22] A. M. Chang, H. U. Baranger, L. N. Pfeiffer, and K. W. West, Phys. Rev. Lett. **73**, 2111 (1994).
[23] J. A. Folk, S. R. Patel, S. F. Godijn, A. G. Huibers, S. M. Cronenwett, C. M. Marcus, K. Campman, and A. C. Gossard, Phys. Rev. Lett. **76**, 1699 (1996).
[24] A. S. Sachrajda, R. Ketzmerick, C. Gould, Y. Feng, P. J. Kelly, A. Delage, and Z. Wasilewski, Phys. Rev. Lett. **80**, 1948 (1998); R. Ketzmerick, Phys. Rev. B **54**, 10 841 (1996).
[25] J. P. Bird, R. Akis, D. K. Ferry, D. Vasileska, J. Cooper, Y. Aoyagi, and T. Sugano, Phys. Rev. Lett. **82**, 4691 (1999).
[26] A. P. Micolich, R. P. Taylor, A. G. Davies, J. P. Bird, R. Newbury, T. M. Fromhold, A. Ehlert, H. Linke, L. D. Macks, W. R. Tribe, E. H. Linfield, D. A. Ritchie, J. Cooper, Y. Aoyagi, and P. B. Wilkinson, Phys. Rev. Lett. **87**, 036802 (2001).
[27] D. Weiss, M. L. Roukes, A. Menschig, P. Grambow, K. von Klitzing, and G. Weimann, Phys. Rev. Lett. **66**, 2790 (1991); R. Fleischmann, T. Geisel, and R. Ketzmerick, *ibid.* **68**, 1367 (1992); D. Weiss, K. Richter, A. Menschig, R. Bergmann, H. Schweizer, K. von Klitzing, and G. Weimann, *ibid.* **70**, 4118 (1993).
[28] K. J. Luo, H. T. Grahn, K. H. Ploog, and L. L. Bonilla, Phys. Rev. Lett. **81**, 1290 (1998).
[29] J. Kastrup, H. T. Grahn, K. H. Ploog, F. Prengel, A. Wacker, and E. Schöll, Appl. Phys. Lett. **65**, 1808 (1994).
[30] K. N. Alekseev, G. P. Berman, D. K. Campbell, E. H. Cannon, and M. C. Cargo, Phys. Rev. B **54**, 10 625 (1996).
[31] T. M. Fromhold, A. A. Krokhin, C. R. Tench, S. Bujkiewicz, P. B. Wilkinson, F. W. Sheard, and L. Eaves, Phys. Rev. Lett. **87**, 046803 (2001).
[32] T. M. Fromhold, L. Eaves, F. W. Sheard, M. L. Leadbeater, T. J. Foster, and P. C. Main, Phys. Rev. Lett. **72**, 2608 (1994).
[33] T. M. Fromhold, P. B. Wilkinson, F. W. Sheard, L. Eaves, J. Miao, and G. Edwards, Phys. Rev. Lett. **75**, 1142 (1995).
[34] T. M. Fromhold, A. Fogarty, L. Eaves, F. W. Sheard, M. Henini, T. J. Foster, P. C. Main, and G. Hill, Phys. Rev. B **51**, 18 029 (1995).
[35] D. L. Shepelyansky and A. D. Stone, Phys. Rev. Lett. **74**, 2098 (1995).
[36] G. Müller, G. S. Boebinger, H. Mathur, L. N. Pfeiffer, and K. W. West, Phys. Rev. Lett. **75**, 2875 (1995).
[37] P. B. Wilkinson, T. M. Fromhold, L. Eaves, F. W. Sheard, N. Miura, and T. Takamasu, Nature (London) **380**, 608 (1996).
[38] T. S. Monteiro and P. A. Dando, Phys. Rev. E **53**, 3369 (1996).
[39] T. M. Fromhold, P. B. Wilkinson, F. W. Sheard, and L. Eaves, Phys. Rev. Lett. **78**, 2865 (1997).
[40] T. M. Fromhold, P. B. Wilkinson, L. Eaves, F. W. Sheard, P. C. Main, M. Henini, M. J. Carter, N. Miura, and T. Takamasu, Chaos, Solitons Fractals **8**, 1381 (1997), special issue on chaos and quantum transport in mesoscopic cosmos, edited by K. Nakamura.
[41] T. S. Monteiro, D. Delande, A. J. Fisher, and G. S. Boebinger, Phys. Rev. B **56**, 3913 (1997).
[42] T. S. Monteiro, D. Delande, J. P. Connerade, Nature (London) **387**, 863 (1997).
[43] E. E. Narimanov, A. D. Stone, and G. S. Boebinger, Phys. Rev. Lett. **80**, 4024 (1998).
[44] E. E. Narimanov and A. D. Stone, Phys. Rev. B **57**, 9807 (1998).
[45] E. E. Narimanov and A. D. Stone, Phys. Rev. Lett. **80**, 49 (1998).
[46] D. S. Saraga and T. S. Monteiro, Phys. Rev. Lett. **81**, 5796 (1998).
[47] D. S. Saraga, T. S. Monteiro, and D. C. Rouben, Phys. Rev. E **58**, 2701 (1998).
[48] D. S. Saraga and T. S. Monteiro, Phys. Rev. E **57**, 5252 (1998).
[49] E. B. Bogomolny and D. C. Rouben, Europhys. Lett. **43**, 111 (1998).
[50] E. B. Bogomolny and D. C. Rouben, Eur. Phys. J. B **9**, 695 (1999).
[51] S. Sridhar and E. J. Heller, Phys. Rev. A **46**, R1728 (1992).
[52] U. Dörr, H.-J. Stöckmann, M. Barth, and U. Kuhl, Phys. Rev. Lett. **80**, 1030 (1998).
[53] U. Kuhl and H.-J. Stöckmann, Phys. Rev. Lett. **80**, 3232 (1998).
[54] J. U. Nöckel and A. D. Stone, Nature (London) **385**, 45 (1997).
[55] C. Gmachl, F. Capasso, E. E. Narimanov, J. U. Nöckel, A. D. Stone, J. Faist, D. L. Sivco, and A. Y. Cho, Science **280**, 1556 (1998).
[56] P. B. Wilkinson, T. M. Fromhold, R. P. Taylor, and A. P. Micolich, Phys. Rev. Lett. **86**, 5466 (2001); Phys. Rev. E **64**, 026203 (2001).
[57] M. L. Leadbeater, F. W. Sheard, and L. Eaves, Semicond. Sci. Technol. **6**, 1021 (1991).
[58] E. J. Heller, Phys. Rev. Lett. **53**, 1515 (1984).
[59] R. K. Hayden, P. B. Wilkinson, T. M. Fromhold, L. Eaves, F. W. Sheard, M. Henini, and N. Miura, Physica B **272**, 163 (2000); Physica E **7**, 735 (2000).
[60] S. Takeyama, H. Ochimizu, S. Sasaki, and N. Miura, Meas. Sci. Technol. **3**, 662 (1992).
[61] M. S. Child, *Semiclassical Mechanics with Molecular Applications* (Oxford University Press, Oxford, 1991).
[62] P. A. Dando and T. S. Monteiro, J. Phys. B **27**, 2681 (1994).